

Signature of supershear transition seen in damage and aftershock pattern

Jorge Jara¹, Lucile Bruhat¹, Solène Antoine², Kurama Okubo³, Marion Y. Thomas⁴, Esteban Rougier⁵, Ares J. Rosakis⁶, Charles G. Sammis⁷, Yann Klinger², Romain Jolivet¹ and Harsha S. Bhat¹.

1. Laboratoire de Géologie, Département de Géosciences, École Normale Supérieure, CNRS, UMR 8538, PSL Research University, Paris, France
2. Institut de Physique du Globe de Paris, Sorbonne Paris Cité, Université Paris Diderot, CNRS, UMR 7154, Paris, France
3. Department of Earth and Planetary Sciences, Harvard University, Cambridge, MA 02138, USA
4. Institut des Sciences de la Terre de Paris, Sorbonne Université, CNRS, UMR 7193, Paris, France
5. EES-17 Earth and Environmental Sciences Division, Los Alamos National Laboratory, Los Alamos, NM, USA
6. Graduate Aerospace Laboratories, California Institute of Technology, Pasadena, California, 91125, USA
7. Department of Earth Sciences, University of Southern California, Los Angeles, CA 90089, USA

Supershear earthquakes are rare but powerful ruptures with devastating consequences. How quickly an earthquake rupture attains this speed, or for that matter decelerates from it, strongly affects high-frequency ground motion and the spatial extent of coseismic off-fault damage^{1–4}. Traditionally, studies of supershear earthquakes have focused on determining which fault segments sustained fully-grown supershear ruptures^{5–9}. Knowing that the rupture first propagated at subshear rupture speeds, these studies usually guessed an approximate location for the transition from subshear to supershear regimes. The rarity of confirmed supershear ruptures^{5–8,10–14}, combined with the fact that conditions for supershear transition are still debated^{2,5,15}, complicates the investigation of supershear transition in real earthquakes. Here, we find a unique signature of the location of a supershear transition: we show that, when a rupture accelerates towards supershear speed, the stress concentration abruptly shrinks, limiting the off-fault damage and aftershock productivity. First, we use theoretical fracture mechanics to demonstrate that, before transitioning to supershear, the stress concentration around the rupture tip shrinks, confining the region where damage & aftershocks are expected. Then, employing two different dynamic rupture modeling approaches, we confirm such reduction in stress concentration, further validating the expected signature in the transition region. We contrast these numerical and theoretical results with high-resolution aftershock catalogs for three natural supershear earthquakes, where we identify a small region with lower aftershock density near the supershear transition. Finally, using satellite optical image correlation techniques, we show that, for a fourth event, the transition zone is characterized by a diminution in the width of the damage zone. Our results demonstrate that the transition from subshear to supershear rupture can be clearly identified by a localized absence of aftershocks, and a decrease in off-fault damage, due to a transient reduction of the stress intensity at the rupture tip.

While the rupture speed of most earthquakes is limited by the speed of the Rayleigh and shear waves, earthquakes can occasionally rupture at higher speeds. These are known as supershear earthquakes. Because the on-fault rupture speed controls the characteristics of the resulting off-fault damage, understanding the conditions for a rupture to transition from the sub-Rayleigh to the supershear regime is critical for earthquake hazard assessment. Abrupt changes in the rupture speed indeed increases high-frequency radiation¹, and governs the spatial extent of the coseismic off-fault damage zone²⁻⁴. Whether supershear ruptures are real or not has been a matter of debate for a long time. Even though theoretical models^{16,17} and laboratory experiments¹⁸ provided evidence that supershear ruptures exist since the early 1970s, it was not until the M_w 6.5 Imperial Valley earthquake (California, 1979) that a supershear rupture was inferred in nature for the first time¹⁰. Pioneering laboratory experiments¹⁹⁻²¹ together with observations from the M_w 7.4 1999 Izmit and the M_w 7.2 1999 Düzce earthquakes in Turkey¹¹, then conclusively confirmed that supershear ruptures are in fact much more common than previously expected. Supershear ruptures have now been inferred for several, albeit rare, events: The M_w 7.8 2001 Kunlun (China) earthquake^{5,12}, the M_w 7.8 2002 Denali (Alaska) earthquake⁶, the M_w 7.5 2013 Craig (Alaska) earthquake¹³, the M_w 6.7 2013 Okhotsk (Kamchatka) earthquake¹⁴ and most recently the M_w 7.5 2018 Palu (Indonesia) earthquake^{7,8}. Efforts have been made in order to identify and characterize these supershear earthquakes using various methodological approaches⁵⁻⁹, where the methods used were in most cases, designed to reveal a posteriori which segment of the rupture propagated at supershear velocities. These methods often ignore the details of the transition to supershear rupture speed. They simply limit themselves to the analysis of full-grown supershear ruptures. When the rupture was known to propagate earlier at subshear speeds, the supershear transition is presumed to have occurred in-between, leading to an imprecise location of this transition. The conditions for supershear transitions in nature are still poorly understood, despite numerical efforts to characterize the mechanics of the transition process^{2,15,22,23}. Here, we present an original signature of a supershear transition by combining theoretical and numerical modeling with field observations (high-resolution aftershock catalogs and surface displacement fields from optical satellite image correlation analyses).

The theoretical analysis is conducted using Linear Elastic Fracture Mechanics which provides closed form solutions to describe the state of stress around a rupture tip. Considering a semi-infinite plain-strain crack in a 2D homogeneous isotropic linear medium, moving at a speed $v < c_R$ (where c_R is the Rayleigh wave speed), the near-tip stress solution is controlled by the dynamic stress intensity factor, K_{II}^{dyn} , which evolves with the rupture speed v . A Lorentz-like contraction of the stress field occurs around the rupture tip as the rupture speed approaches its limiting speed, c_R ²⁴. This contraction has also been observed and verified experimentally²⁵. For an earthquake rupture transitioning to a supershear regime, the rupture has to first accelerate to the Rayleigh wave speed. As the rupture approaches the supershear transition, K_{II}^{dyn} monotonically decreases to zero, strongly reducing the stress concentration at the rupture tip. Thus the off-fault domain affected by this stress concentration will also shrink (see Methods section

for details). We illustrate this effect by calculating the extent of the region where the stress state goes beyond the limits defined by a Drucker-Prager failure criterion (Figs. 1a and 1b). This domain, which describes the theoretical extent of coseismic off-fault deformation, such as fracture damage and aftershocks, will be directly affected by stress changes. As the rupture approaches the Rayleigh wave speed, with uniform (Fig. 1a) or non-uniform (Fig. 1b) rupture velocity, the stress concentration at the rupture tip eventually collapses, limiting the spatial extent of possible off-fault damage and aftershocks during the transition from the sub-Rayleigh to the supershear regime.

This theoretical demonstration is then validated through two different numerical models that account for dynamic evolution of coseismic damage^{3,4}. In these models, unlike the theoretical development presented above, the rupture is spontaneous and there is a feedback between off-fault damage and on-fault rupture. Both models produce in-plane dynamic simulations of an earthquake rupture on a 1D right-lateral planar fault embedded in a 2D medium. A slip-weakening friction law is used to model the earthquake rupture and damage only occurs on the tensional part of the fault (bottom side of the fault on Fig. 1c and d). The first model employs enhanced numerical algorithms for earthquake rupture allowing for spontaneous activation of off-fault fracture networks⁴. This has been observed in experiments as well²⁶. Once the rupture is over, we evaluate the damage pattern and the spatial variation of closeness to failure (ΔCF) resulting from the rupture. Regions with positive values of ΔCF are more likely to host fracture damage and trigger future aftershocks. We see that the regions experiencing sub-Rayleigh and full blown supershear regimes manifest high local stress fluctuations (Fig. 1c). However, when the rupture is transitioning to supershear speed, $\Delta CF \sim 0$, and the spatial extent of the off-fault damage zone drops dramatically. The second numerical model accounts for off-fault damage using a micro-mechanics based effective constitutive law³. The resulting off-fault damage density, which is directly affected by the near-tip stress state, as illustrated by the ΔCF , is also characterized by a sudden shrinkage of the damage zone (Fig. 1d) during the supershear transition (see Methods section for details).

Assuming that the nucleation of early near-fault aftershocks (occurring around a week after the main earthquake) is mainly governed by the stress state left in the wake of the earthquake, we analyze the spatial and temporal distribution of relocated aftershocks for 3 well-known supershear ruptures: The M_w 7.4 1999 Izmit (Turkey) earthquake^{9,11} (Fig. 2a), the M_w 7.9 2002 Denali (Alaska) earthquake⁶ (Fig. 2d), and the M_w 7.5 2013 Craig (Alaska) earthquake¹³ (Fig. 2g). For these examples, we compute the seismic moment released by the aftershocks at a distance of less than 5 km from the main fault, and, for different periods of time after the main shock: 1-3 days, 1, 2, 3 weeks and 1 month (Figs. 2 c, f, and i). In each case, we observe a region of limited extent (~ 5 km) characterized either by reduced seismic moment, and by a clear lack of aftershocks (Fig. 2 b, c, e, f, h and i, pink boxes). This feature is persistent, no matter the distance considered when computing the cumulative seismic moment (see Supplementary Information Figures S3-S14). Note that the systematic increment observed on the cumulative seismic moment, in the transition region, after 3 weeks might be related to postseismic deformation, as the maximum afterslip is actually co-located for

each event in the inferred transition region^{27–29}. It suggests that the gap in the early aftershocks productivity (less than 3 weeks after the mainshock) is mainly related to the supershear transition (see Methods section for details).

As high-resolution aftershocks catalogs are not available for all the supershear earthquake ruptures, we explore a new method to investigate the spatial evolution of the damage zone width. Recent developments in satellite optical image analysis and sub-pixel correlation methods now allow for the detection of displacement variations due to an earthquake down to a resolution of one meter. Noting that, for earthquakes of large magnitudes ($M_w \geq 7$), fault zones (fault core and damage zone) are usually of metric- to kilometric-scale³⁰, we apply this method to the M_w 7.8 2001 Kunlun (China) earthquake^{2,5,12}. Displacement profiles normal to the fault are computed using pre- and post-earthquake images and are used to infer the width of the fault zone (fault core and damage zone Fig. 3). While the overall mean of the fault zone width is around 238 meters, we observe a clear localized region, ~ 11 km-long, where damage largely reduced down to a mean of 127 meters, located around what was previously inferred as the supershear transition zone⁵. As expected from numerical modeling, the supershear transition is characterized by a significant reduction in damage zone width (see Methods section for details). We acknowledge here that the aftershock catalog of Robinson and colleagues¹² also alludes to the same conclusion. However due to the lack of high spatio-temporal density of aftershocks in their catalog we instead chose the above technique.

Theoretical and numerical modeling of off-fault damage both show that the transition from the sub-Rayleigh to the supershear regime is characterized by a reduction in the width of the damage zone and a paucity of aftershocks. This results from the transient shrinkage in stress concentration around the rupture tip as its velocity approaches the Rayleigh wave speed. We cross-validate this predicted feature, with seismological evidence of aftershock quiescence for the Izmit, Denali and Craig supershear earthquakes, and with geodetic observations of the damage zone for the Kunlun earthquake. These results are valid for a well-developed sub-Rayleigh rupture that transitions to supershear speeds. Recent observations from the Palu earthquake hint that the rupture might have either nucleated directly at a supershear speed, or transitioned very early on^{7,8}. For this particular case, further exploration is required to see if similar features can be observed in the field. In conclusion, identifying an absence of aftershocks and decrease in off-fault damage allows us to pinpoint the transition from sub-Rayleigh to supershear speeds. This work provides a new framework to better characterize supershear transition zones in the field, and further explore the mechanical conditions for such transitions.

References

- [1] Das, S. The Need to Study Speed. *Science* **317**, 905–906 (2007).
- [2] Bhat, H. S., Dmowska, R., King, G. C., Klinger, Y. & Rice, J. R. Off-fault damage patterns due to supershear ruptures with application to the 2001 Mw 8.1 Kokoxili (Kunlun) Tibet earthquake. *J. Geophys. Res.* **112**, 1–19 (2007).
- [3] Thomas, M. Y. & Bhat, H. S. Dynamic evolution of off-fault medium during an earthquake: A micromechanics based model. *Geophys. J. Int.* **214**, 1267–1280 (2018).
- [4] Okubo, K. *et al.* Dynamics, radiation and overall energy budget of earthquake rupture with coseismic off-fault damage. *J. Geophys. Res.* **124**, 1–41 (2019).
- [5] Vallée, M., Landès, M., Shapiro, N. M. & Klinger, Y. The 14 November 2001 Kokoxili (Tibet) earthquake: High-frequency seismic radiation originating from the transitions between sub-Rayleigh and supershear rupture velocity regimes. *J. Geophys. Res.* **113**, 1–14 (2008).
- [6] Ellsworth, W. L. *et al.* Near-Field Ground Motion of the 2002 Denali Fault, Alaska, Earthquake Recorded at Pump Station 10. *Earthq. Spectra* **20**, 597–615 (2004).
- [7] Bao, H. *et al.* Early and persistent supershear rupture of the 2018 magnitude 7.5 Palu earthquake. *Nature Geoscience* **12**, 200–205 (2019).
- [8] Socquet, A., Hollingsworth, J., Pathier, E. & Bouchon, M. Evidence of supershear during the 2018 magnitude 7.5 Palu earthquake from space geodesy. *Nature Geoscience* **12**, 192–199 (2019).
- [9] Bouchon, M. & Karabulut, H. The aftershock signature of supershear earthquakes. *Science* **320**, 1323–1325 (2008).
- [10] Archuleta, R. J. A faulting model for the 1979 Imperial Valley earthquake. *J. Geophys. Res.* **89**, 4559–4585 (1984).
- [11] Bouchon, M. *et al.* How fast is rupture during an earthquake? New insights from the 1999 Turkey earthquakes. *Geophys. Res. Lett.* **28**, 2723–2726 (2001).
- [12] Robinson, D. P., Brough, C. & Das, S. The Mw 7.8, 2001 Kunlunshan earthquake: Extreme rupture speed variability and effect of fault geometry. *J. Geophys. Res.* **111**, 1–10 (2006).
- [13] Yue, H. *et al.* Supershear rupture of the 5 January 2013 Craig, Alaska (Mw7.5) earthquake. *J. Geophys. Res.* **118**, 5903–5919 (2013).

- [14] Zhan, Z., Helmberger, D. V., Kanamori, H. & Shearer, P. M. Supershear rupture in a Mw 6.7 aftershock of the 2013 Sea of Okhotsk earthquake. *Science* **345**, 204–207 (2014).
- [15] Bruhat, L., Fang, Z. & Dunham, E. M. Rupture complexity and the supershear transition on rough faults. *J. Geophys. Res.* **121**, 210–224 (2016).
- [16] Burridge, R. Admissible Speeds for Plane-Strain Self-Similar Shear Cracks with Friction but Lacking Cohesion. *Geophys. J. Int.* **35**, 439–455 (1973).
- [17] Andrews, D. J. Rupture velocity of plane strain shear cracks. *J. Geophys. Res.* **81**, 5679–5687 (1976).
- [18] Wu, F. T., Kuenzler, H. & Thomson, K. C. Stick-slip propagation velocity and seismic source mechanism. *Bull. Seism. Soc. Am.* **62**, 1621–1628 (1972).
- [19] Rosakis, A. J., Samudrala, O. & Coker, D. Cracks Faster than the Shear Wave Speed. *Science* **284**, 1337–1340 (1999).
- [20] Xia, K. W., Rosakis, A. J. & Kanamori, H. Laboratory Earthquakes: The Sub-Rayleigh-to-Supershear Rupture Transition. *Science* **303**, 1859–1861 (2004).
- [21] Passelegue, F. X., Schubnel, A., Nielsen, S., Bhat, H. S. & Madariaga, R. From Sub-Rayleigh to Supershear Ruptures During Stick-Slip Experiments on Crustal Rocks. *Science* **340**, 1208–1211 (2013).
- [22] Liu, Y. & Lapusta, N. Transition of mode II cracks from sub-Rayleigh to intersonic speeds in the presence of favorable heterogeneity. *J. Mech. Phys. Solids* **56**, 25–50 (2008).
- [23] Liu, C., Bizzarri, A. & Das, S. Progression of spontaneous in-plane shear faults from sub-rayleigh to compressional wave rupture speeds. *J. Geophys. Res.* **119**, 8331–8345 (2014).
- [24] Freund, L. B. Crack propagation in an elastic solid subjected to general loading-ii. non-uniform rate of extension. *J. Mech. Phys. Solids* **20**, 141–152 (1972).
- [25] Svetlizky, I. Fineberg, J. Classical shear cracks drive the onset of dry frictional motion. *Nature* **509**, 205–208 (2014).
- [26] Rosakis, A. J. Intersonic shear cracks and fault ruptures. *Adv. Phys.* **51**, 1189–1257 (2002).
- [27] Freed, A. M., Bürgmann, R., Calais, E., Freymueller, J. & Hreinsdóttir, S. Implications of deformation following the 2002 Denali, Alaska, earthquake for postseismic relaxation processes and lithospheric rheology. *J. Geophys. Res.* **111**, B01401 (2006).

- [28] Hearn, E. H., McClusky, S., Ergintav, S. & Reilinger, R. E. Izmit earthquake postseismic deformation and dynamics of the North Anatolian Fault Zone. *J. Geophys. Res.* **114**, B08405 (2009).
- [29] Ding, K., Freymueller, J. T., Wang, Q. & Zou, R. Coseismic and Early Postseismic Deformation of the 5 January 2013 Mw 7.5 Craig Earthquake from Static and Kinematic GPS Solutions. *Bull. Seism. Soc. Am.* **105**, 1153–1164 (2015).
- [30] Gold, R. D. *et al.* On- and off-fault deformation associated with the September 2013 Mw 7.7 Balochistan earthquake: Implications for geologic slip rate measurements. *Tectonophysics* **660**, 65–78 (2015).

Supplementary Information is available in the online version of the paper.

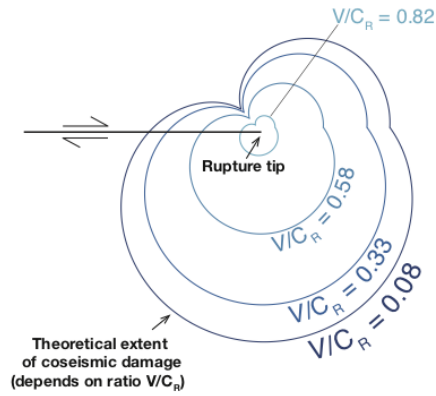
Acknowledgements J.J. and R.J. acknowledge the funding of the European Research Council (ERC) under the European Union's Horizon 2020 research and innovation program (grant agreement 758210, project Geo4D). L.B. thanks the funding from the People Programme (Marie Curie Actions) of the European Union's Seventh Framework Programme (FP7/2007-2013) under REA grant agreement PCOFUND-GA-GA-2013-609102, through the PRESTIGE programme coordinated by Campus France. S.A. and Y.K. are partly supported by the ANR project DISRUPT (ANR-18-CE31-0012).

Author Contributions H.S.B. conceived, designed and supervised the project. J.J. performed the aftershock analysis. L.B. and H.S.B. conducted the theoretical study. S.A. did the image correlation. K.O., E.R., M.T. and H.S.B. conducted the numerical analysis. J.J., L.B. and H.S.B. wrote the manuscript. All the authors contributed to the analysis, interpretation and manuscript preparation.

Author Information Reprints and permissions information is available at www.nature.com/reprints. The authors declare no competing financial interests. Readers are welcome to comment on the online version of the paper. Correspondence and requests for materials should be addressed to J.J. (jara@geologie.ens.fr).

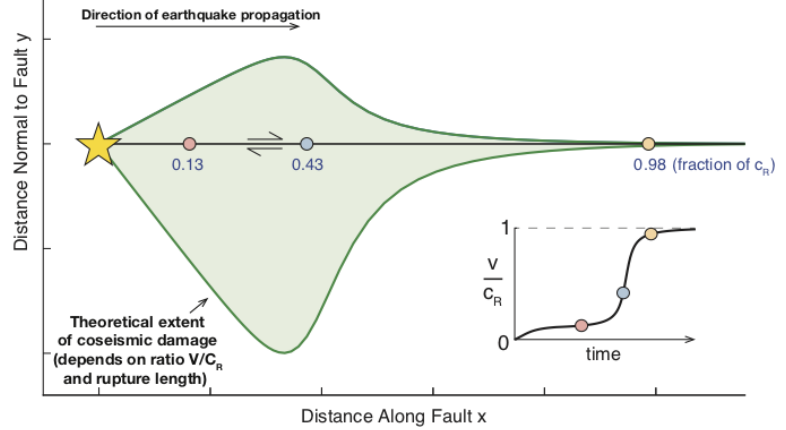
a.

Domain of potential damage (Drucker-Prager failure criterion) for a crack propagating with uniform rupture velocity

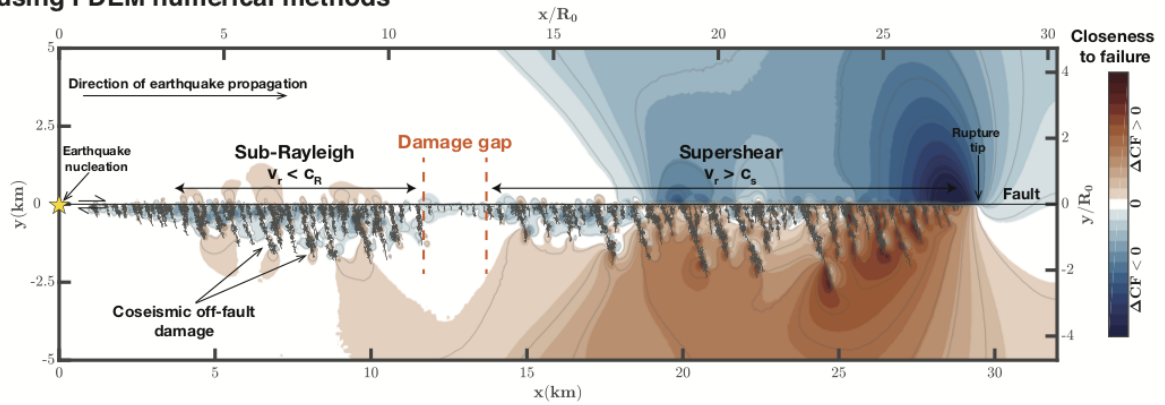


b.

Domain of potential damage (Drucker-Prager failure criterion) for a crack propagating with non-uniform rupture velocity



c. Closeness to failure and coseismic off-fault fracture pattern of a supershear transition using FDEM numerical methods



d. Closeness to failure and damage pattern of a supershear transition using a homogenized law for microcracks

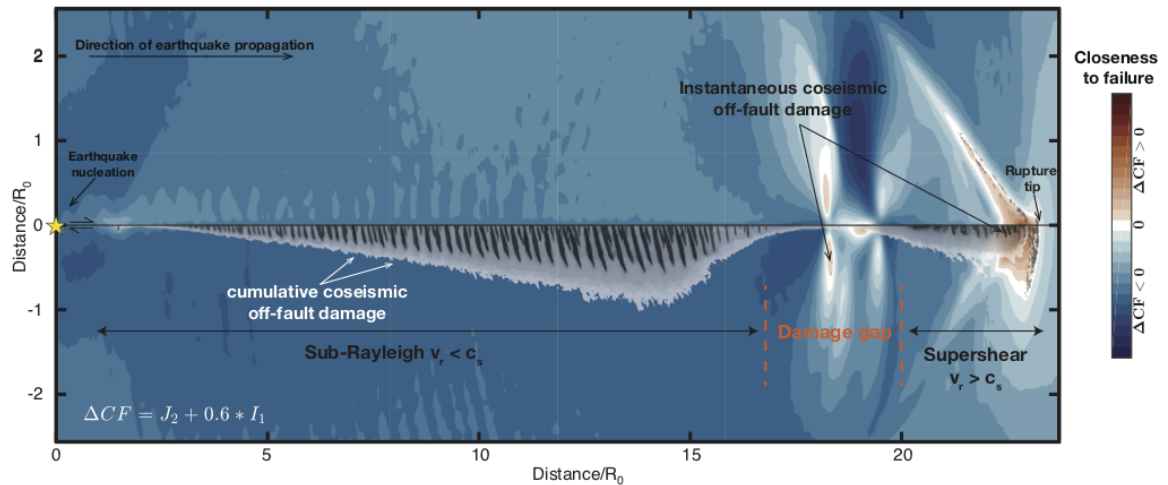


Figure 1: Theoretical and Numerical Evidence of Supershear Transition Signature. **a. & b.** Domain that exceeds Drucker-Prager failure criterion for a crack of uniform rupture velocity (**a**) and for a crack of non-uniform rupture velocity (**b**). Both cases show that the region of potential damage shrinks as the rupture velocity v approaches the Rayleigh wave speed c_R . **c.** Changes in closeness to failure associated with Drucker-Prager failure criterion, computed using 2D FDEM dynamic simulation including coseismic off-fault damage generated by the rupture propagation⁴. **d.** Same as (**c**) but using an effective medium theory³. The grey regions map the spatial distribution of damage density that occurs during the entire event while the black field record the damage that takes place at the time at which the Drucker-Prager failure criterion was computed. In both cases (**c** & **d**), regions of positive change are more likely to host fracture damage and trigger future aftershocks. The transition from the sub-Rayleigh to the supershear regime is clearly denoted by a more localized and weaker stress perturbation and a consequent gap in damage.

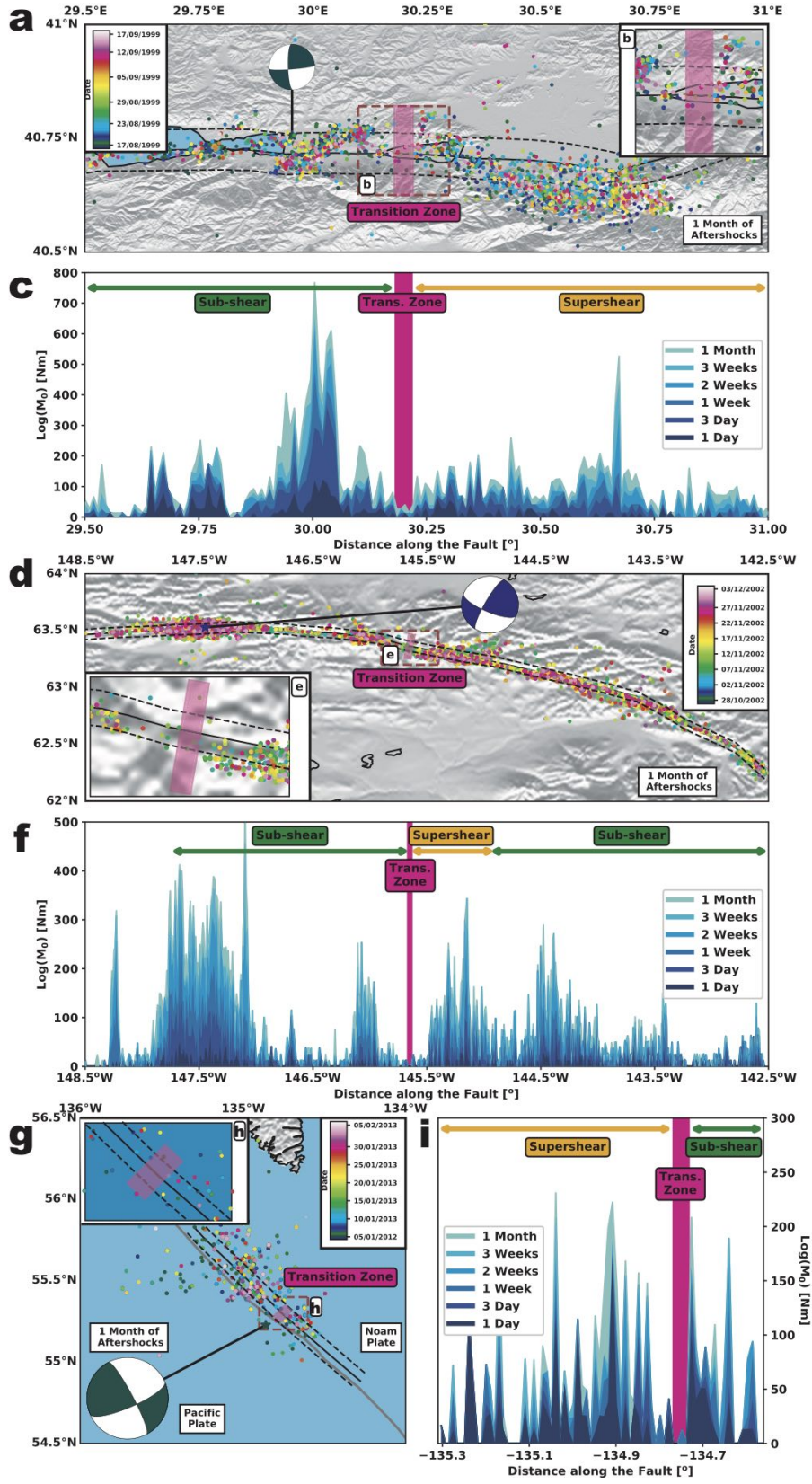


Figure 2

Figure 2: High-Resolution Aftershock Catalog Analysis. 1-month aftershock distribution for Izmit (**a**), Denali (**d**), and Craig (**g**) earthquakes, color-coded by time and indicating the respective event epicenter (color-coded star) and focal mechanism. The black continuous line denotes the surface rupture for each event. **c,f,i** Cumulative aftershock seismic moment release projected on the main fault (in log scale) at different temporal scales (1-3 days, 1-2-3 weeks and 1 month), for Izmit (**c**), Denali (**f**), and Craig (**i**) earthquakes. All the aftershocks within a distance of 5 km from the fault are considered in the calculation (area denoted by the black discontinuous lines in **a**, **d** and **g**). Color-coded arrows indicate the different speed regimes reported for each event (green for sub-Rayleigh and orange for supershear)^{6,9,13}, while the pink boxes indicate this work's proposed Transition Zones. **b,e,h** Zoom plot of the region proposed as Transition zone in this study for each earthquake.

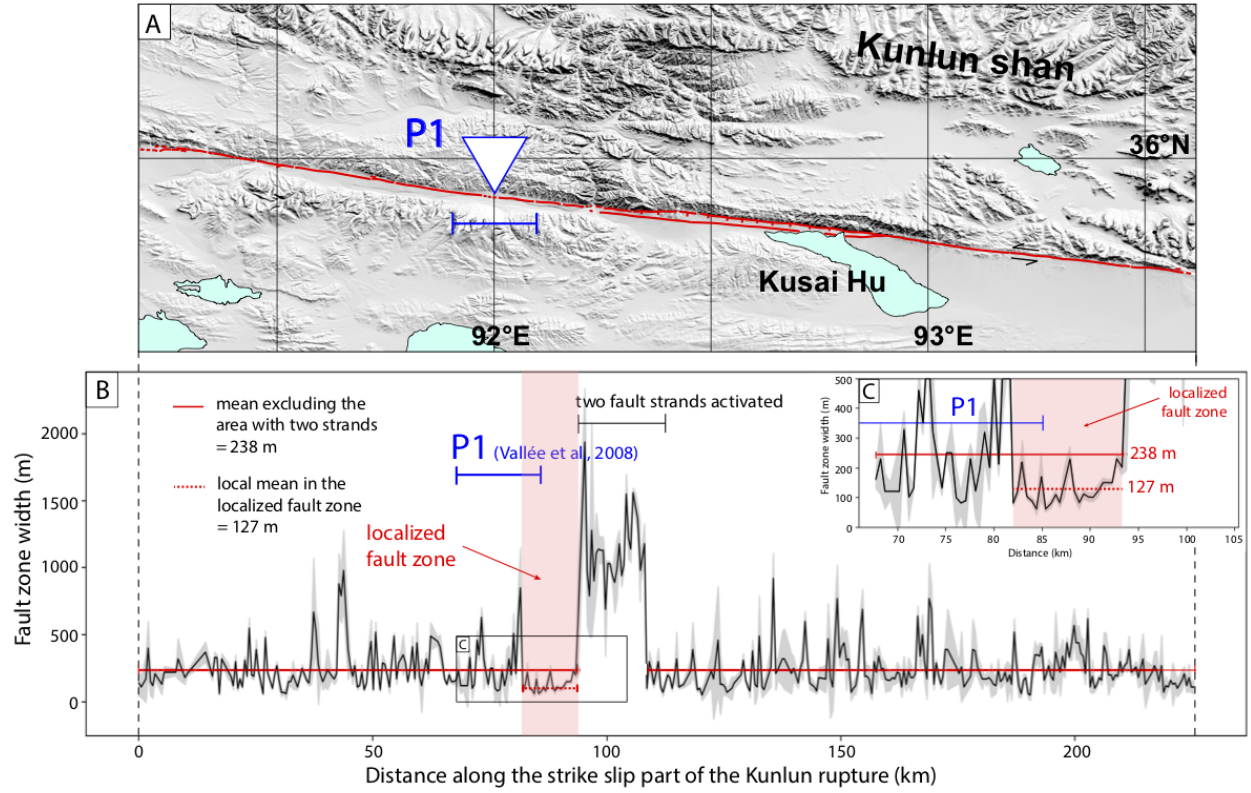


Figure 3: Optical Correlation Images Analysis. **a.** Map of the strike slip section of the M_w 7.8 2001 Kunlun (China) earthquake, where P1 denotes the transition zone reported for the event from seismological far-field data⁵. **b.** Along-Strike fault zone width (black) and its associated uncertainty (grey), obtained from the analysis of 40 km-long profiles, sampling the fault zone every 500 m, on the surface displacement maps. The latter is derived from correlating pre- and post-earthquake SPOT 1-4 images. The 11 km-long red area highlighted the specific region with a mean fault width (red dashed line) of only 127 m compared to 238 m recorded for the rest of the rupture (red line). The latter excludes the area where two parallel fault strands are activated and for which the fault zone is exceptionally large (> 1000 m). **c.** Zoom of the Fig. 3 **b**.

Methods

Linear elastic fracture mechanics solution

The variability of earthquake rupture speed affects the high-frequency content generation^{1,31} and the activation of the coseismic off-fault damage²⁻⁴. We develop an approximation to understand how the velocity grows during a seismic rupture using the Linear Elastic Fracture Mechanics approach. In a 2D homogeneous isotropic linear-elastic body, we consider a semi-infinite plain-strain crack of length L , and (r, θ) polar coordinates centered at the crack tip. The static near-tip stress $\sigma_{\alpha\beta}$ field is given by

$$\sigma_{\alpha\beta}(r, \theta) = \frac{K_{II}}{\sqrt{2\pi r}} f_{\alpha\beta}^{II}(\theta) \quad (1)$$

where K_{II} is the static stress intensity factor and $f_{\alpha\beta}^{II}$ are universal angular functions^{32,33}. The static stress intensity factor varies with the crack length such that

$$K_{II} = \phi(\sigma, \tau) \sqrt{\pi L} \quad (2)$$

where $\phi(\sigma, \tau)$ depends on the applied normal σ and shear τ stress. The stress at the rupture tip increases then with the crack length.

Now consider that the crack tip moves at a speed $v \leq c_R$, where c_R is the Rayleigh wave speed. The near-tip stresses now depend on the rupture speed v as follows

$$\sigma_{\alpha\beta}(r, \theta, v) = \frac{K_{II}^{dyn}(v)}{\sqrt{2\pi r}} f_{\alpha\beta}^{II}(\theta, v) \quad (3)$$

where K_{II}^{dyn} is the dynamic stress intensity factor. This solution is entirely analogous to the static problem. However, due to the moving coordinate system, all the fields undergo a Lorentz-like contraction, affecting both the stress intensity factor and the angular distribution. The dynamic stress intensity factor can be approximated as²⁴

$$K_{II}^{dyn} \approx \frac{1 - v/c_R}{\sqrt{1 - v/c_P}} K_{II} \quad (4)$$

where c_P is the limiting speed for a mode II crack, being c_P the P-wave speed. Also $K_{II} = \phi(\sigma, \tau) \sqrt{\pi L(t)}$ where the crack length is given by $L(t) = \int_0^t v(t) dt$.

Using the expressions above, we will compute the extent of the ‘yield’ region in the off-fault medium. To generalize and illustrate the state of stress, we represent normal and shear stress by their invariants

$$I_1 = \frac{\sigma_{kk}}{3} \quad \text{and} \quad J_2 = \sqrt{\frac{1}{2} s_{ij} s_{ji}} \quad \text{with} \quad s_{ij} = \sigma_{ij} - I_1 \delta_{ij} \quad (5)$$

Solutions from linear elastic fracture mechanics give the state of stress at the crack tip for a mode II crack:

$$\sigma_{11} + \sigma_{22} = \frac{K_{II}}{\sqrt{2\pi r}} \sin \frac{\theta}{2}. \quad (6)$$

Since $\sigma_{33} = \nu(\sigma_{11} + \sigma_{22})$, where ν Poisson's ratio, we can compute the stress invariant I_1 :

$$I_1 = \frac{1 + \nu}{3} \frac{K_{II}}{\sqrt{2\pi r}} \sin \frac{\theta}{2}. \quad (7)$$

Likewise, we compute s_{12} :

$$s_{12} = \sigma_{12} \quad (8)$$

$$= \frac{K_{II}}{\sqrt{2\pi r}} \left[\cos \frac{\theta}{2} \left(1 - \sin \frac{\theta}{2} \sin \frac{3\theta}{2} \right) \right] \quad (9)$$

The bracketed term is designated as $A(\theta)$. The resulting second invariant of the stress deviator J_2 is

$$J_2 = \sqrt{\frac{1}{2} s_{12}^2}, \quad (10)$$

$$= \frac{K_{II}}{\sqrt{2\pi r}} |A(\theta)|. \quad (11)$$

Using the corresponding Drucker-Prager failure criterion F with a friction coefficient f , we define the yield region, i.e. the extent of the region where the stress state goes beyond the limits defined by the Drucker-Prager failure criterion.

$$F = J_2 - f I_1, \quad (12)$$

$$= \frac{K_{II}}{\sqrt{2\pi r}} \left[\frac{1}{2} |A(\theta)| - f \frac{1 + \nu}{3} \sin \frac{\theta}{2} \right]. \quad (13)$$

We label the bracketed term as $\sqrt{B(\theta, \nu, f)}$:

$$F \equiv \frac{K_{II}}{\sqrt{2\pi r}} \sqrt{B(\theta, \nu, f)}. \quad (14)$$

We can then derive the maximum distance r_{DP} at which the Drucker-Prager failure criterion $F = 0$ is reached:

$$r_{DP}(\theta, \nu, f) = \frac{K_{II}^2 B(\theta, \nu, f)}{2\pi F^2} \quad (15)$$

Now consider that the crack is moving at a speed v . The stress intensity factor K_{II} becomes K_{II}^{dyn} , defined in equation (4). Also, one can assume that the static intensity tensor is given by $K_{II} = \Delta\tau\sqrt{\pi L}$, so that we can update the distance r_{DP} for a moving crack:

$$r_{DP}(\theta, \nu, f, v) = \frac{(1 - v/c_R)^2}{(1 - v/c_P)} L(t) \frac{\Delta\tau^2 B(\theta, \nu, f)}{2F^2} \quad (16)$$

For an accelerating crack, the extent of the yield region r_{DP} is then a combined effect of the increase in L due to crack growth and the decrease of the term $(1 - v/c_R)^2/(1 - v/c_P)$ with increasing speed.

Numerical dynamic simulations including off-fault coseismic damage

Several efforts has been made to understand the supershear ruptures from a dynamic perspective^{2,22,34,35}. However, models accounting for off-fault coseismic change damage has only been recently developed, and should now be used

to explore complex feedback that exist between this particular type of rupture dynamic and the surrounding medium. Here we employ two approaches to simulate dynamic earthquake ruptures: one based on the finite discrete element method (FDEM)⁴ and another one based on a constitutive model that accounts for the dynamic evolution of elastic moduli at high-strain rates³.

FDEM modeling

To reproduce coseismic damage, we use the software suite HOSSedu, developed by the Los Alamos National Laboratory (LANL)³⁶. The numerical algorithms behind this tool are based on the combined Finite-Discrete Element Method (FDEM) to produce dynamically activated off-fault fracture networks. One of the key FDEM is to allow each individual interface between the finite elements describing the off-fault medium to have their own tensional and shear cohesion. Furthermore, these interfaces can break under appropriate stress conditions. Each broken interface is then assimilated to a damage fracture. When the rupture propagates, this allows for a live build-up of the damage patterns^{4,37}.

Closeness to failure is derived using the invariant form of the Mohr-Coulomb yield criterion:

$$F_{MC} \equiv J_2 R_{MC} - I_1 \tan \phi - C_{II}^p \quad (17)$$

where $\tan \phi = f_s$ is initial static friction coefficient and C_{II}^p is initial peak shear cohesion. Failure occurs when $F_{MC} \geq 0$. Note that when $R_{MC} = 1$, the above become the Drucker-Prager yield criterion.

Here,

$$R_{MC} = \frac{1}{\sqrt{3} \cos \phi} \sin \left(\Theta + \frac{\pi}{3} \right) + \frac{1}{3} \cos \left(\Theta + \frac{\pi}{3} \right) \tan \phi ; \quad \Theta = \frac{1}{3} \cos^{-1} \left(\frac{r}{J_2} \right)^3 \quad (18)$$

where $r = \left(\frac{9}{2} S_{ij} S_{jk} S_{ki} \right)^{\frac{1}{3}}$.

The closeness to failure yields

$$\Delta CF(\mathbf{x}, t) = \frac{F_{MC}(\mathbf{x}, t)}{F_{MC}^0(\mathbf{x}, t)} - 1. \quad (19)$$

Here F_{MC}^0 is the Mohr-Coulomb yield function for the initial, uniform, state of stress. Failure is more likely to occur when $\Delta CF > 0$. (See Table S1 for all the parameters used in the simulations).

During the supershear transition, the intensity and spatial extent of off-fault damage drops (Fig 1). In fact, while both the sub-Rayleigh and the supershear segments present high fluctuations of the stress invariants I_1 and J_2 , the transitional region is clearly depleted in stress changes (Fig. S1).

Micromechanics approach

The second numerical method, reflects the micro-physics of damage evolution by relating damage density to the near-tip stress state and by computing the corresponding dynamic changes of elastic properties in the medium due to the

presence of newly formed cracks.

Here, closeness to failure ΔCF is simply derived using the Drucker-Prager yield criterion:

$$\Delta CF(\mathbf{x}, t) = \frac{F_{MC}(\mathbf{x}, t)}{F_{MC}^0(\mathbf{x}, t)} - 1 \quad \text{with} \quad F_{MC} \equiv J_2 - I_1 \tan \phi, \quad (20)$$

where $\tan \phi = f_s = 0.6$ is initial static friction coefficient. Failure is more likely to occur when $\Delta CF > 0$.

Aftershock Catalog Analysis

We have studied three well known supershear ruptures for which high-resolution aftershock catalogs are available, at least 1-month after the main event. The M_w 7.4 1999 Izmit earthquake^{11,38} had a mean rupture velocity of ~ 4.8 km/s, and a well-recorded 3-month aftershock catalog⁹ (Fig. 2a for 1-month aftershock locations and Figs. S3-S6 for spatiotemporal evolution of the aftershocks). In the case of the M_w 7.8 2002 Denali (Alaska) earthquake, velocities of ~ 5.5 km/s have been reported^{6,39}, but in this case, 1-year aftershocks catalog has been published⁴⁰ (Fig. 2d for 1-month aftershock locations and Figs. S7-S10 for spatiotemporal evolution of the aftershocks). Finally, the M_w 7.5 2013 Craig (Alaska) earthquake was pinpointed as a supershear event, with velocities of 5.5 - 6.0 km/s, that lasted for around 100 km. For the earthquake analysis we have used a 5 month-long aftershock catalog⁴¹ (Fig. 2g for 1-month aftershock locations and Figs. S11-S14 for spatiotemporal evolution of the aftershocks).

Subpixel correlation methods for damage fault width

The M_w 7.8 2001 Kunlun (China) earthquake^{2,5,12,42,43} is a very well known supershear rupture, but unfortunately the seismic network in the region was poor developed, being studied only by teleseismic data. Because of it, we are not able to apply the high-resolution aftershock analysis developed in the main text. On the other hand, this earthquake was well recorded by satellite images, that allows us to explore the size of the off-fault coseismic damage zone using optical correlation images techniques.

We used SPOT 1 to 4 images, covering the Kunlun fault area from 1988 to 2004 with a ground resolution of 10 meters, allowing for a change detection larger than a meter^{30,46-48}. The correlation of pre- and post-earthquake paired images is done using MicMac^{44,45}, measuring the horizontal surface displacement between the two optical acquisitions.

We focused on the central part of the rupture, dominated by fault parallel motion, excluding the two eastern and western ends where fault normal and thrust components are respectively acting. Using the tool Stacking profiles from ENVI version 5.5.1 (Exelis Visual Information Solutions, Boulder, Colorado), 460 stacked profiles were placed perpendicular to the fault trace every 500 meters along the analysed section (stacked profiles are rectangles of 40 km-long and 1 kilometer wide in which individual slip profiles are stacked allowing to reduce noise and artefacts). On each

profile, it is possible to observe the coseismic offset produced by the earthquake (See Supplementary Information, Fig. S15, for a profile example) where the width of this offset corresponds to the fault's zone width (including fault core and damage zone), that is computed over 396 clear-enough profiles along the fault trace, allowing to draw a fault zone width curve (Fig. 3).

Two different means for the fault zone width are calculated (red and dashed red lines in Fig. 3). One is at 238 meters and corresponds to the mean of the fault zone width for the whole area of study, however removing the partitioning zone with two fault strands. The second one, at 127 meters, corresponds to the mean of a fault zone width where slip localizes for 11 km-long, located next to what was defined as the supershear transition using seismological data⁵.

References

- [31] Madariaga, R. High frequency radiation from dynamic earthquake. *Ann. Geophys.* **1**, 17 (1983).
- [32] Freund, L. B. The mechanics of dynamic shear crack propagation. *J. Geophys. Res.* **84**, 2199 (1979).
- [33] Williams, M. L. On the stress distribution at the base of a stationary crack. *J. Appl. Mech.* **24**, 109–114 (1975).
- [34] Dunham, E. M., Favreau, P. & Carlson, J. M. A Supershear Transition Mechanism for Cracks. *Science* **299**, 1557–1559 (2003).
- [35] Dunham, E. M. Conditions governing the occurrence of supershear ruptures under slip-weakening friction. *J. Geophys. Res.* **112**, 1–24 (2007).
- [36] Rougier, E., Knight, E. E., Lei, Z. & Munjiza, A. HOSS.edu2.x (Hybrid Optimization Software Suite - Educational Version, Second Generation) (2016).
- [37] Klinger, Y. *et al.* Earthquake damage patterns resolve complex rupture processes. *Geophys. Res. Lett.* (2018).
- [38] Bouchon, M. *et al.* Seismic imaging of the 1999 Izmit (Turkey) rupture inferred from the near-fault recordings. *Geophys. Res. Lett.* **27**, 3013–3016 (2000).
- [39] Dunham, E. M. & Archuleta, R. J. Evidence for a supershear transient during the 2002 Denali fault earthquake. *Bull. Seism. Soc. Am.* **94**, S256—S268 (2004).
- [40] Ratchkovski, N. A. *et al.* Aftershock Sequence of the Mw 7.9 Denali Fault, Alaska, Earthquake of 3 November 2002 from Regional Seismic Network Data. *Seismol. Res. Lett.* **74**, 743–752 (2003).
- [41] Holtkamp, S. & Ruppert, N. A high resolution aftershock catalog of the magnitude 7.5 Craig, Alaska, earthquake on 5 January 2013. *Bull. Seism. Soc. Am.* **105**, 1143–1152 (2015).
- [42] Bouchon, M. & Vallée, M. Observation of Long Supershear Rupture During the Magnitude 8.1 Kunlunshan Earthquake. *Science* **301**, 824–826 (2003).
- [43] Vallée, M. & Dunham, E. M. Observation of far-field Mach waves generated by the 2001 Kokoxili supershear earthquake. *Geophys. Res. Lett.* **39**, n/a–n/a (2012).
- [44] Rosu, A.-M., Pierrot-Deseilligny, M., Delorme, A., Binet, R. & Klinger, Y. Measurement of ground displacement from optical satellite image correlation using the free open-source software MicMac. *ISPRS J. Photogramm. Remote Sens.* **100**, 48–59 (2015).

- [45] Rupnik, E., Daakir, M. & Pierrot Deseilligny, M. MicMac – a free, open-source solution for photogrammetry. *Open Geospatial Data, Software and Standards* **2**, 14 (2017).
- [46] Tchalenko, J. S. & Ambraseys, N. N. Structural analysis of the Dasht-e Bayaz (Iran) earthquake fractures. *Bull. Geol. Soc. Am.* (1970).
- [47] Vallage, A., Klinger, Y., Grandin, R., Bhat, H. & Pierrot-Deseilligny, M. Inelastic surface deformation during the 2013 Mw 7.7 Balochistan, Pakistan, earthquake. *Geology* **43**, G37290.1 (2015).
- [48] Mitchell, T. & Faulkner, D. The nature and origin of off-fault damage surrounding strike-slip fault zones with a wide range of displacements: A field study from the Atacama fault system, northern Chile. *Journal of Structural Geology* **31**, 802–816 (2009).